ACS APPLIED MATERIALS & INTERFACES

www.acsami.org

Research Article

Multifunctional Magnetothermo-Responsive Smart Hydrogel for On-Demand Controlled Drug Release in Cancer Therapy

Zahra Moazzami Goudarzi, Sohrab Asgaran, Magdalena Osial, Njemuwa Nwaji, Dorota Kołbuk, Arkadiusz Gradys, Bartlomiej Kalaska, Olga Urbanek, and Paweł Sajkiewicz*

Cite This: https://doi.org/10.1021/acsami.6c10083

Read Online

ACCESS | Metrics & More | Article Recommendations | Supporting Information

ABSTRACT: Targeted and on-demand drug delivery technologies have attracted considerable interest for personalized cancer therapies. In this study, we developed a UV-crosslinkable and thermo-responsive gelatin methacrylate (GelMa)—poly(N-isopropylacrylamide) (PNIPAM) (G/P) hybrid hydrogel, integrated with folic acid-functionalized superparamagnetic iron oxide nanoparticles (SPIONs). Differential scanning calorimetry (DSC) and alternating magnetic field (AMF) evaluations confirmed that introducing GelMa modulated the lower critical solution temperature (LCST) to approximately 32 °C while enabling efficient magnetothermal response. Cyclic compression tests demonstrated superior mechanical properties. The 2.5G/P hydrogel achieved a compressive strength of 0.06 MPa at 78% strain, outperforming pure GelMa (0.023 MPa) and PNIPAM (0.012 MPa), with the highest modulus of elasticity at both 25 and 37 °C. *In vitro* biocompatibility assays using L929 fibroblasts indicated excellent cytocompatibility with >70% viability over 7 days. Furthermore, the hydrogel demonstrated excellent blood compatibility with a hemolysis ratio below 2%, complying with ISO 10993-4 standards. Synergistic reduction in cell viability was observed in human lung adenocarcinoma (NCI-H1975) and fibroblast-like osteosarcoma (MG-63) cell lines when combining drug loading and simulated AMF thermal stimulation. Triggered by hyperthermia at 41 °C, the hydrogel demonstrated a highly controlled, pulsatile 'ON/OFF' drug release profile of 5-fluorouracil (5-FU) driven by network shrinkage, achieving a maximum cumulative release of 72.6% over 28 days with a well-defined biphasic kinetic pattern. These results show that this dual-stimuli responsive hydrogel is a mechanically robust, highly efficient platform for controlled cancer therapy.

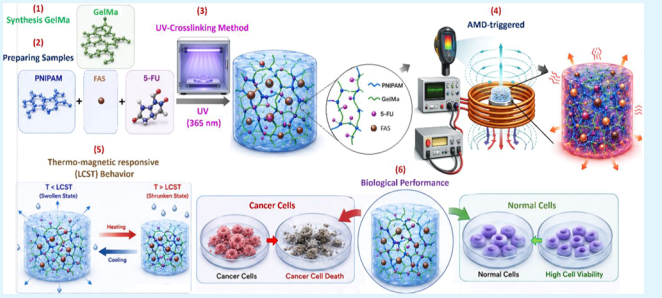

KEYWORDS: *UV-crosslinkable hydrogels, thermo-magnetic responsive hydrogels, cancer-targeting nanoplatforms, superparamagnetic iron oxide nanoparticles (SPIONs), AMF-triggered drug release, biocompatibility*

INTRODUCTION

As a widespread health crisis characterized by uncontrolled cell mutations, cancer remains a leading cause of death globally across all demographic groups. Projections for 2025 estimate 2 million new cases in the United States, with nearly half involving breast, lung, prostate, or colorectal cancers.[1] Modern cancer treatment utilizes a multidisciplinary approach combining surgery, radiotherapy, and chemotherapy, sometimes incorporating precise tools like laser therapy or focused ultrasound for specialized tissues. While drug administration is a fundamental therapeutic method, its success depends less on a drug's inherent potency and more on its ability to effectively reach the target site. Challenges in drug delivery significantly influence overall efficacy by impacting critical factors such as pharmacokinetics, toxicity, and cellular uptake.[2]

While conventional systems focused on sustained drug delivery, modern research has shifted toward on-demand, controlled release to enable precise timing, location, and dosage for personalized therapies. The success of these systems relies on a spatio-temporal approach that maintains optimal drug concentrations at the target site while minimizing systemic side effects.[3−5] Among various polymer systems investigated as drug delivery platforms, hydrogels are increasingly favored due to their high porosity, three-dimensional structure, and ability to absorb significant amounts of physiological fluids. Hydrogel materials offer unique advantages, such as tissue adhesion, biodegradability, the ability to mimic the extracellular matrix, and, above all, the ability to respond to external stimuli.[6−9] In recent years, hydrogels have emerged as a highly versatile class of biomaterials, showcasing a remarkable diversity in chemical

Received: May 19, 2026
Revised: July 22, 2026
Accepted: July 22, 2026

compositions, cross-linking mechanisms, and processing methodologies to meet the stringent demands of biomedical applications. Recent comprehensive reviews have extensively documented this expanding landscape, detailing the transition from conventional networks to highly tailorable and advanced functional hydrogel platforms.[10,11]

Stimuli-responsive hydrogels change their shape or volume as a result of structural or chemical transitions in response to external stimuli, being physical (temperature, light, electric/magnetic field), chemical (pH, glucose), or biological (enzymes). These changes make on-demand drug release possible directly on the target site.[12−16]

Poly(N-isopropylacrylamide) (PNIPAM) has been well investigated as a typical thermosensitive material due to its reversible phase transition at the lower critical solution temperature (LCST), which is 32 °C in aqueous solution.[17,18] At temperatures below the LCST, PNIPAM is hydrophilic with chains in the form of flexible, expanded coils. At temperatures above LCST, the PNIPAM chains collapse into globules, becoming hydrophobic.[19] Researchers have verified thermoresponsive hydrogels based on PNIPAM for a flexible drug delivery patch dedicated to wound healing or cancer treatment, enabling controlled drug release by exploiting PNIPAM's LCST behavior.[20−22] So far, PNIPAM has been combined with both gold nanorods and magnetic nanoparticles in order to prepare thermoresponsive microgels or hydrogels.[2,23,24]

A natural way to overcome some of the problems associated with using pure PNIPAM is to create hybrid systems using natural polymers. The addition of natural polymers like gelatin improves the mechanical properties of PNIPAM and bioactivity, as well as increases the biodegradability of the system. In the case of gelatin, the effect is more pronounced after its modification with methacrylic anhydride, resulting in the formation of gelatin methacrylate (GelMa). GelMa is a very useful form of gelatin due to the possibility of being photo-crosslinked in the presence of a photoinitiator, resulting in the formation of three-dimensional structures under UV.[25−28] This property is crucial for stabilization of the material after injection into a body. Moreover, GelMa effectively prevents the entire scaffold from collapsing above the PNIPAM LCST temperature. Furthermore, the addition of GelMa increases the LCST of the resulting hydrogel. This shift is primarily driven by the change in the hydrophilic-hydrophobic balance of the polymer chains. The introduction of a large number of polar functional groups into the system by the addition of GelMa results in stronger bonds with water molecules, which require more thermal energy to break these bonds and force the polymer to collapse into its hydrophobic state.

GelMa-based thermoresponsive composites have been analyzed so far by various groups, including the development of G/P hybrid systems exhibiting temperature-induced phase transitions and reversible volume changes under physiological conditions.[29,30] For instance, Huang et al. engineered a thermoresponsive G/P bilayer hydrogel actuator in which the incorporation of PNIPAM introduced an LCST-driven phase transition, resulting in pronounced and reversible volumetric deformation upon thermal stimulation. The mismatch in swelling behavior between the GelMa and PNIPAM layers enabled temperature-triggered actuation without compromising the structural integrity of the construct.[29] Similarly, Daaboul et al. reported GelMa/NIPAm hybrid hydrogels exhibiting cyclic swelling–deswelling behavior at physiologically relevant temperatures, demonstrating controlled modulation of network permeability and water content across thermal transitions. These systems highlight how the integration of thermosensitive polymeric segments into GelMa matrices can impart externally regulated thermoresponsive behavior while preserving the biocompatibility and photocrosslinkable characteristics of the GelMa backbone.[30]

So far, e.g., Li et al.[24]studied the physico-chemical properties of the PNIPAM and GelMa combination dedicated to the fabrication of microscale vasculatures and verified its biocompatibility on human umbilical vein endothelial cells and osteosarcoma cells, both *in vitro* and *in vivo*. It was found that the G/P hydrogels' sizes and shrinkage ratios could be well-controlled by regulating GelMa concentration. Cell studies confirmed the biocompatibility of G/P hydrogels in a 7-day experiment, as well as CD31 marker expression, which confirmed the maintenance of endothelial function. More complex material systems containing GelMa and PNIPAM were also proposed. Liu et al. proposed multifunctional thermal and magnetic microcarriers (TMMs) made of PNIPAM, polylysines (PLLs), GelMa, poly (ethylene glycol) diacrylate (PEGDA), N,N-methylenebis(acrylamide) (MBA), Fe_3O_4 and SiO_2.[31] Also, PNIPAM and GelMa polymer systems were studied in combination with different nanoparticles so far, e.g., graphene oxide nanoparticles.[32,33]

An additional possibility for triggering the drug release is the introduction of nanoparticles in the form of gold nanoparticles or superparamagnetic iron oxide nanoparticles (SPIONs). In both cases, the mechanism of drug release triggering is related to a local increase in temperature by an external stimulus. In the case of gold nanoparticles, near-infrared light is an effective stimulus, while for SPION, an alternating magnetic field (AMF) is effective to induce local hyperthermia even for relatively deep-located tissues. SPIONs are approved not only for stimulation of hyperthermia but also for diagnostic purposes by magnetic resonance imaging (MRI).[34−39] Dagdelen et al. demonstrated the incorporation of SPIONs into a redox-responsive degradable microgel system, showcasing their ability to induce controlled drug release under hyperthermic conditions. Their responsiveness to an alternating magnetic field enables precise, non-invasive activation, proving SPIONs' potential for targeted and on-demand therapeutic applications.[40] The nanocomposite design approach can determine whether release occurs via controlled drug bursts or by up-regulating release kinetics over an extended period, with up to 20-fold ON/OFF state resolution already reported.[41]

So far, few researchers have analyzed the material system containing G/P and SPIONs for on-demand drug delivery. Jalili et al. prepared an injectable drug delivery system, composed of iron oxide nanoparticles coated with PNIPAM and loaded with doxorubicin (DOX). These drug nanocarriers were entrapped within a GelMa prepolymer solution before crosslinking. The studies aimed to analyze on-demand drug delivery and *in vitro* efficacy using osteoblasts and osteosarcoma cells. On-demand local drug delivery using magnetothermal activation was confirmed.[42] The significantly enhanced release at higher temperatures was observed, particularly above the LCST transition, confirming the temperature-triggered behavior of the injectable hydrogel. The presented data showed that ca. 75.1% of the loaded DOX was released after 24 h of thermal exposure above the LCST transition temperature. A lower release at 37 °C was observed in samples containing the

https://doi.org/10.1021/acsami.6c10083
ACS Appl. Mater. Interfaces XXXX, XXX, XXX−XXX

GelMa matrix compared to samples composed of nanogels only, indicating a significant influence of the local environment on drug release dynamics.

The reaction of aldehyde-functionalized dextran with hydrazide-functionalized PNIPAM-coated SPIONs was used by Campbell et al. to prepare an injectable, degradable, in situ gelling hydrogel nanocomposite in which SPIONs are covalently grafted into the hydrogel network structure.[43,44] However, this type of linkage can restrict the mobility of SPIONs, resulting in an inhomogeneous response during heating.

Here, we propose a stimuli-responsive system made of folic acid-functionalized SPIONs (FAS) physically integrated within a G/P hydrogel matrix. The physical encapsulation of FAS enhances nanoparticle mobility, thereby promoting uniform heat dissipation when activated by an AMF. Furthermore, leveraging FAS as thermal actuators induces the controlled deswelling of the thermoresponsive hydrogel, creating additional free volume within the matrix, which subsequently facilitates accelerated drug release through external AMF modulation.

RESULTS AND DISCUSSION

A novel G/P hydrogel was synthesized by the radical grafting of UV-crosslinkable GelMa with thermo-responsive PNIPAM via sequential N-acylation with UV-crosslinkable moiety (methacrylate groups) based on rational design and selection protocol (Figure 1), and the as-prepared hydrogel was subsequently utilized for controlled AMF-triggered localized drug release. Prior to the preparation of the hybrid hydrogel, the GelMa precursor was prepared via the reaction of gelatin methacrylic anhydride using the method described in the literature.[45,46] ^{1}H-NMR spectral signals confirmed successful GelMa formation, exhibiting chemical shifts at around 5.4 and 5.6 ppm, which were assigned to the acrylic protons (2H) of the grafted methacrylate group. In contrast, the signal at 1.9 ppm was attributed to the methyl group (3H) of the grafted methacrylate group (Figure S1).

Samples used in this study and their component concentrations are detailed in Table 1.

The SEM analysis of G/P hydrogels (Figure 2A) revealed a spongy structure with macro- and micropores, with undulating grooves. Such interconnected pore networks mimicking the extracellular matrix (ECM) are crucial from the perspective of tissue regeneration, supporting the effective diffusion of oxygen, nutrients, and metabolic by-products.

In G/P hydrogels, an increase of GelMa from 1.5 to 3.5% (w/w) led to a significant increase in pore size, from 279.5 ± 17.63 to 1068.12 ± 89.81 μm. As shown in Figure 2B, the average pore size for pure GelMa is 332.73 ± 19.44 μm, which is consistent with the literature report.[46,47] Compared to GelMa, the PNIPAM hydrogel exhibited a higher pore size, reaching 926.90 ± 39.87 μm, which falls below the macropore size observed in the higher-concentration GelMa hydrogel. The hybrid 2.5G/P and 2.5G/PFAS hydrogels displayed a porous structure with both macro- and micropore structures intermeshed, indicating the blending of GelMa, PNIPAM, and FAS. The significant increase in pore diameter following the cross-linking of GelMa with PNIPAM renders the hydrogel suitable for cell growth and endows the hydrogel with better mechanical strength.

The structural characteristics of the hybrid hydrogel were analyzed using FTIR spectroscopy, as shown in Figure 2C. The spectrum of GelMa alone exhibits characteristic peaks of gelatin polymer with an absorption band around 3346 cm^{-1}, which can be attributed to the O–H and N–H stretching vibrations. In contrast, peaks in the region 2800–3100 cm^{-1} can be assigned to the stretching vibration of C–H groups. The

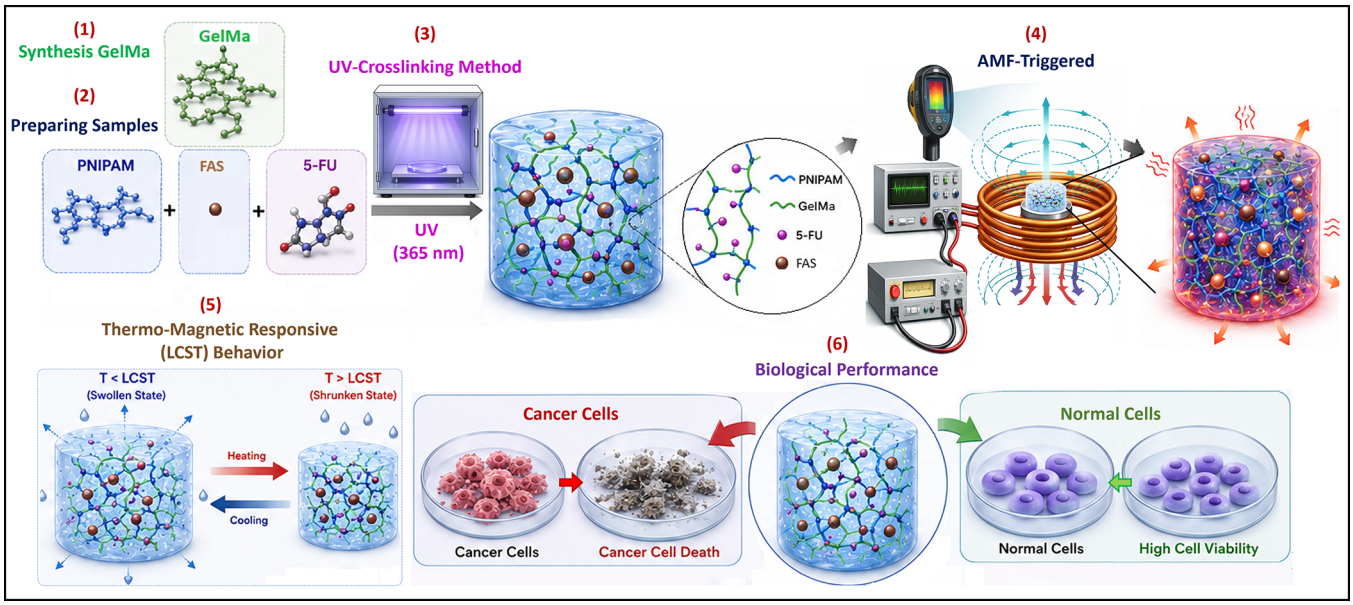

Figure 1. Schematic illustration of the preparation, structure, and multifunctional behavior of the thermomagnetic responsive hydrogel system for AMF-triggered drug delivery and anticancer therapy. (1,2) Chemical structure of synthesized GelMa, PNIPAM, FAS, and 5-FU; (3) formation of the UV-crosslinked hybrid hydrogel integrating GelMa, PNIPAM, and therapeutic agents (FAS and 5-FU); (4) application of AMF generating localized thermal stimulation via FAS, enabling controlled and on-demand drug release, (5) thermo-responsive volume phase transition of the hydrogel below and above the LCST, regulating swelling/deswelling behavior; and (6) mechanism of selective anticancer performance: combined drug-thermal therapy inducing targeted tumor cell death with minimal toxicity to normal cells.

https://doi.org/10.1021/acsami.6c10083
ACS Appl. Mater. Interfaces XXXX, XXX, XXX–XXX

Table 1. Samples Characteristics

name	GelMa % (w/w)	PNIPAM % (w/w)	FAS % (w/w of polymer mass)	5-FU % (w/w of polymer mass)
GelMa	10	0	0	0
PNIPAM	0	5	0	0
1.5G/P	1.5	5	0	0
2.5G/P	2.5	5	0	0
3.5G/P	3.5	5	0	0
2.5G/PFAS	2.5	5	2	0
2.5G/P-1/2D	2.5	5	0	0.5
2.5G/P-D	2.5	5	0	1
2.5G/PFAS-1/2D	2.5	5	2	0.5
2.5G/PFAS-D	2.5	5	2	1

gelatin-based backbone structure is associated with the absorption bands observed at 1630 cm^{-1} (C=O stretching, amide I) and 1537 cm^{-1} (N–H bending coupled to C–H stretching, amide II).[48] Similarly, the typical characteristic peaks of PNIPAM were observed at 1542, 1639, and 3294 cm^{-1}, which can be ascribed to N-H bending, C=O stretching, and secondary amide (N–H) stretching, respectively.[27] The spectra of the hybrid hydrogel with different ratios of the G/P combination were almost identical due to the overlapping of characteristic peaks of PNIPAM and GelMa with some peak shift arising from cross-linking. However, a slight shift was observed in the characteristic peaks of individual PNIPAM and GelMa compared to the hybrid hydrogel, which can be attributed to the hydrogen bonding between PNIPAM and GelMa. Incorporating FAS into the hydrogel does not show any noticeable change in the FTIR spectra, suggesting that FAS is trapped within the hydrogel matrix without forming covalent bonds.

The hydrogels' thermal behavior was analyzed using differential scanning calorimetry (DSC), as shown in Figure 2D. The DSC heating scans reveal that pure GelMa aqueous solution does not exhibit any thermal effect within the studied temperature range, while pure PNIPAM solution displays an endothermic peak starting at 25 °C and ending at 40 °C with a maximum at 32 °C. According to the literature, this peak is associated with PNIPAM's transition from a random coil to a globular structure.[49] The incorporation of GelMa into the hydrogel significantly reduces the magnitude of the transition peak from 25 to 2.5 J g_{PNIPAM}^{-1} and shifts the peak to higher temperatures, for example, to 41 °C for the 3.5 G/P formulation. Moreover, the addition of FAS to the 2.5 G/P hydrogel results in a slight decrease in the transition temperature by 1 °C while nearly doubling the peak size from 6 to 10 J g_{PNIPAM}^{-1}, indicating an alteration in the thermal properties and interactions within the hybrid network.

The morphology studies using transmission electron microscopy (TEM) revealed the uniform spherical shape for the bare SPIONs and FAS, see Figure 2E,F. The size of prepared SPIONs and FAS is below 12 nm, which could be due to the use of hydrochloric acid (HCl) during the coprecipitation synthesis that reduces the size of NPs compared to the SPIONs obtained without additional acidic agent[50] to maintain fine morphology, well-distribution of the NPs in the thermoresponsive polymer matrix, and potential low aggregation post-stimuli treatment. Figure 2G shows the hydrodynamic size of the FAS, where the inset reveals the Zeta potential for the FAS measured in phosphate-buffered saline (PBS) at pH 7.4.

Based on the SEM and DSC results, the 2.5G/P sample composition has been selected for further experiments. This sample is characterized by optimal LCST near physiological conditions and a suitable pore size.

Thermogravimetric analysis provided information on the thermal stability of the material before and after the incorporation of FAS into the hydrogel matrix (Figure 3A). The thermograms for 2.5G/P and 2.5G/P-D before the FAS loading into the hydrogel differ from 2.5G/PFAS and 2.5G/PFAS-D. This difference can be attributed to the presence of FAS in the structure, which acts as heat mediators, enhancing water loss and contributing to hydrogel degradation. The first derivative thermogravimetry (DTG) demonstrates a multi-peak region below 250 °C, originating most probably from the water evaporation that may undergo different kinetics for varied compositions of the material, resulting in different interactions between particular molecules.[51] The main DTG peak for water evaporation in all samples appears below 100 °C, while FAS incorporation results in additional hydrogen bonds between the water molecules and the organic coat as well as the 5-FU in the hydrogel, resulting in an additional peak at 150 °C and its shift to 230 °C. The following DTG exothermic peaks allocated around 400 °C can be ascribed to the degradation of the organic ingredients through decarboxylation and carbonization. As the measurements are performed in a nitrogen atmosphere, the pyrolysis can undergo what is seen at higher temperatures, where the minor peaks above 800 °C are seen. Overall, the presence of FAS leads to a shift in the degradation peaks, indicating its influence on the thermal behavior of the hydrogel matrix.

As the FAS are used as heat generators to enhance drug delivery, their magnetic properties were investigated using a vibrating magnetometer (VSM). The M-H curves of SPIONs, PFAS, and the 2.5G/PFAS composite, measured between −1 and 1 T, exhibit the characteristic shape of superparamagnetic behavior (Figure 3B). The 2.5G/PFAS sample shows a lower saturation magnetization (Ms) compared to both SPIONs and PFAS, as expected due to the increased proportion of organic matrix relative to the magnetic core. Despite this reduction, the overall superparamagnetic trend is preserved, which is promising for AMF-triggered drug release via magnetic hyperthermia, as it reduces the risk of nanoparticle aggregation after drug release. Figure 3C shows thermographic images of the hydrogel captured using a thermal imaging camera at AMF amplitudes of 27 and 33 G.

Figure 3D illustrates the temperature-induced volume shrinkage of PNIPAM and 2.5G/P-D hydrogels during heating to 40 °C, illustrating the thermoresponsive volume phase transition behavior after 5-FU encapsulation. Additionally, the magnetically induced heating and energy conversion capability of the 2.5G/PFAS-D hybrid hydrogel were evaluated by exposing the sample to an AMF. Figure 3E,F presents the temperature-time profiles of the 2.5G/PFAS-D suspension under different AMF intensities, showing uniform heating behavior across the sample. The temperature gradually increases with increasing magnetic field strength, reaching maxima of 31, 33, and 41 °C

https://doi.org/10.1021/acsami.6c10083
ACS Appl. Mater. Interfaces XXXX, XXX, XXX–XXX

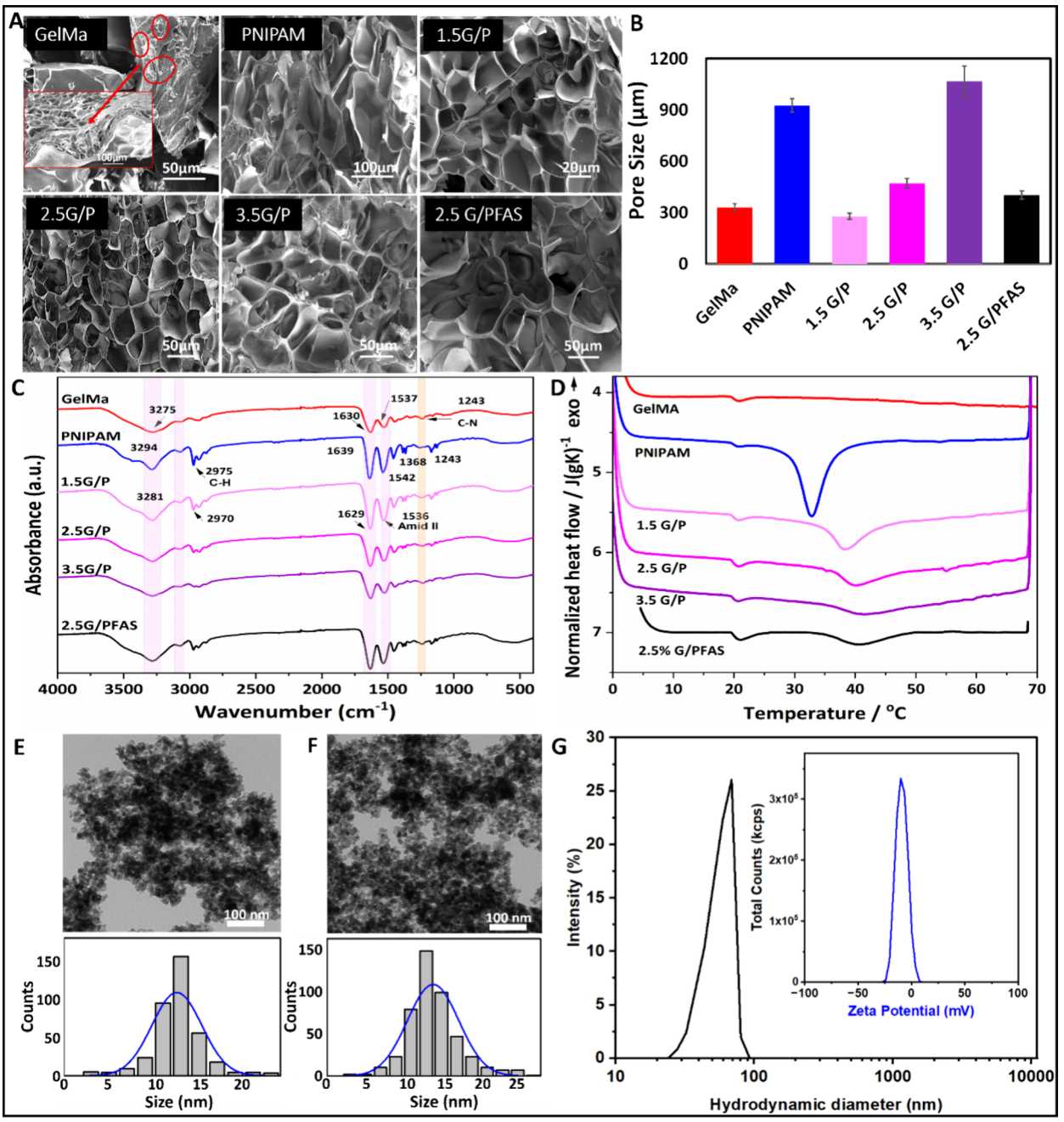

Figure 2. (A) SEM images of GelMa, PNIPAM, 1.5 G/P, 2.5 G/P, 3.5 G/P, and 2.5 G/PFAS thermoresponsive hydrogels; (B) TEM images of SPIONs and FAS; (C) corresponding pore area; (C) FTIR spectra of the thermoresponsive hydrogels; and (D) examples of DSC scans for various compositions registered upon heating at 10 K min^{-1}; a note: a small endothermic peak seen at 20 °C on presented DSC scans is an instrumental artifact occurring also on the DSC baseline scan; TEM images and histograms for (E) SPIONs, (F) FAS, and (G) hydrodynamic size of FAS, where inset shows the Zeta potential of the FAS in pH 7.4.

within 800 s at 14, 22, and 27 G, respectively. At 33 G, the temperature stabilizes around 40 °C, while 35 G raises it to 43 °C (Figure 3E). It is worth noting that samples at the therapeutic temperature are achieved by 10 min of AMF application, and applied conditions are below the acceptable body limit in small regions of about 1.8×10^9 A m^{-1} s^{-1}, reducing the risk of generation of eddy currents.[52−54]

It has been shown that a temperature of 40–42 °C does not cause any damage at the cellular level.[55−57] Thus, the 27 G intensity that produces a temperature of 41 °C was considered worthy of further study. Temperature-time profiles measured at four different spots of the hydrogel under AMF at 27 G nearly overlap (Figure 3F), indicating homogeneous SPION distribution and consistent heating.

https://doi.org/10.1021/acsami.6c10083
ACS Appl. Mater. Interfaces XXXX, XXX, XXX−XXX

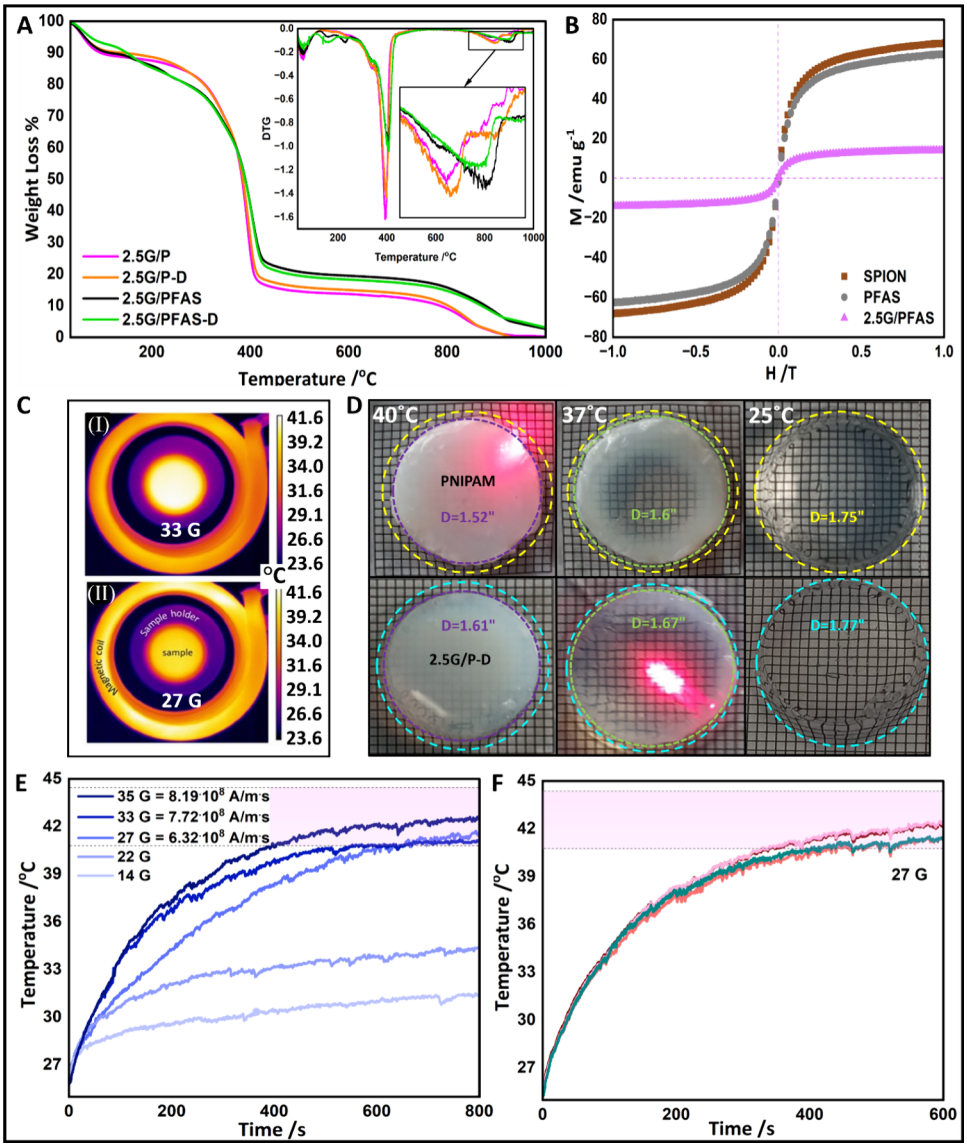

Figure 3. (A) Thermograms for investigated hydrogels, with and without FAS, where inset shows DTG curves and particular range of temperatures in detail, (B) M–H curves, (C) images from the thermovision camera of tested hydrogel at 33 and 27 G amplitude of AMF, (D) temperature-induced volume shrinkage of PNIPAM and 2.5G/P-D hydrogels, (E) 2.5G/PFAS-D hydrogel under alternating magnetic fields with amplitudes ranging from 14 to 35 G, and (F) temperature profiles of 2.5G/PFAS hydrogel under 27 G AMF.

Furthermore, UV spectrophotometric analysis of the incubation medium did not reveal characteristic absorption peaks corresponding to FAS release during the investigated period, suggesting stable nanoparticle retention within the hydrogel matrix.

The cyclic compression tests, conducted at both 25 and 37 °C, further highlight the mechanical robustness and shape recovery of the 2.5 G/P hydrogel (Figure 4A,B). The results indicate that the 2.5 G/P hydrogel maintained consistent mechanical performance across all cycles at both temperatures, demonstrating its stability and durability under repetitive stress conditions. At body temperature (37 °C), both PNIPAM and the 2.5 G/P hydrogel exhibited similar strain behavior during cycling; however, the 2.5 G/P hydrogel showed significantly higher stress levels, indicating a greater capacity to withstand mechanical forces without deformation. At room temperature (25 °C), the 2.5 G/P hydrogel demonstrated higher stress levels compared to GelMa and PNIPAM, but with reduced strain. This suggests that the 2.5 G/P formulation provides a more rigid structure while retaining flexibility to resist mechanical fatigue. This enhanced mechanical profile, especially at physiological temperature, highlights its suitability. The mechanical properties of the biohybrid hydrogels with different G/P mass ratios demonstrate that the 2.5 G/P hydrogel possesses superior compressive strength, achieving 0.06 MPa at 78% compression strain, compared to pure GelMa (0.023 MPa) and PNIPAM (0.012 MPa) (Figure 4C and D). Additionally, the 2.5 G/P hydrogel exhibited the highest modulus of elasticity at both room temperature (25 °C) and body temperature (37 °C) (Figure 4E), likely due to a higher degree of chemical cross-linking interactions between GelMa and PNIPAM.

https://doi.org/10.1021/acsami.6c10083
ACS Appl. Mater. Interfaces XXXX, XXX, XXX–XXX

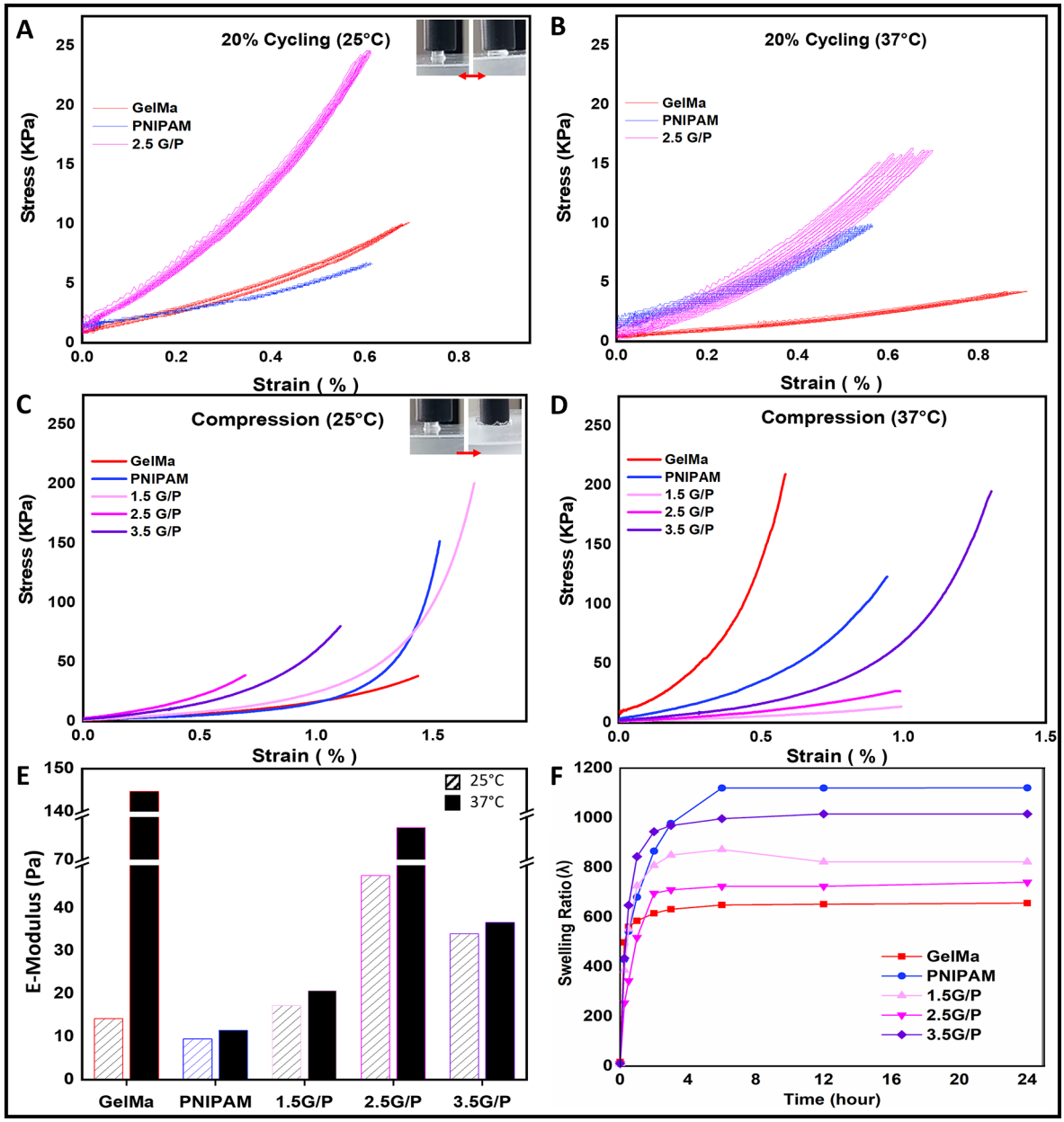

Figure 4. (A,B) Cycling behavior of GelMa, PNIPAM, and 2.5 G/P hybrid hydrogels in PBS solution at 25 and 37.5 °C; (C,D) compression stress vs. strain; (E) elastic modulus at 25 and 37.5 °C; and (F) swelling ratio of thermoresponsive hydrogel samples.

A key parameter in determining the drug release kinetics of the hydrogel is the swelling behavior. The swelling behavior of the as-prepared hydrogels was investigated in the PBS buffer (pH 7.4) at 25 °C. It is pertinent to note that the ionic strength plays a key role in influencing the swelling behavior. In the swelling experiment, the ionic strength of the PBS buffer is expected to reduce the osmotic pressure difference between the hydrogel network and the surrounding solution, thereby lowering the equilibrium swelling ratio.[58] As shown in Figure 4F, PNIPAM exhibits the highest swelling ratio, whereas GelMa shows the lowest value. The G/P hybrid hydrogels display intermediate swelling behavior, with the equilibrium swelling ratio increasing with GelMa content. For all samples, a rapid increase in swelling is observed during the initial hours of immersion, followed by a plateau corresponding to the equilibrium swelling state.[59]

The L929 fibroblasts, which are adherent cells responsible for extracellular matrix production, displayed similar morphology in extracts of the hydrogels and on TCP (tissue culture plastic) (Figure 5). The cell proliferation in the presence of the hydrogel solution did not show any difference compared to the control solution, and an increase in cell density with time was consistently observed. After 24 h, the fibroblasts maintained their typical shape and well-spread morphology, extending filopodia and lamellipodia, indicative of required cell-material interactions.

Previous AMF-heating measurements confirmed that the 2.5G/P hydrogel reached the magnetothermally relevant

https://doi.org/10.1021/acsami.6c10083
ACS Appl. Mater. Interfaces XXXX, XXX, XXX–XXX

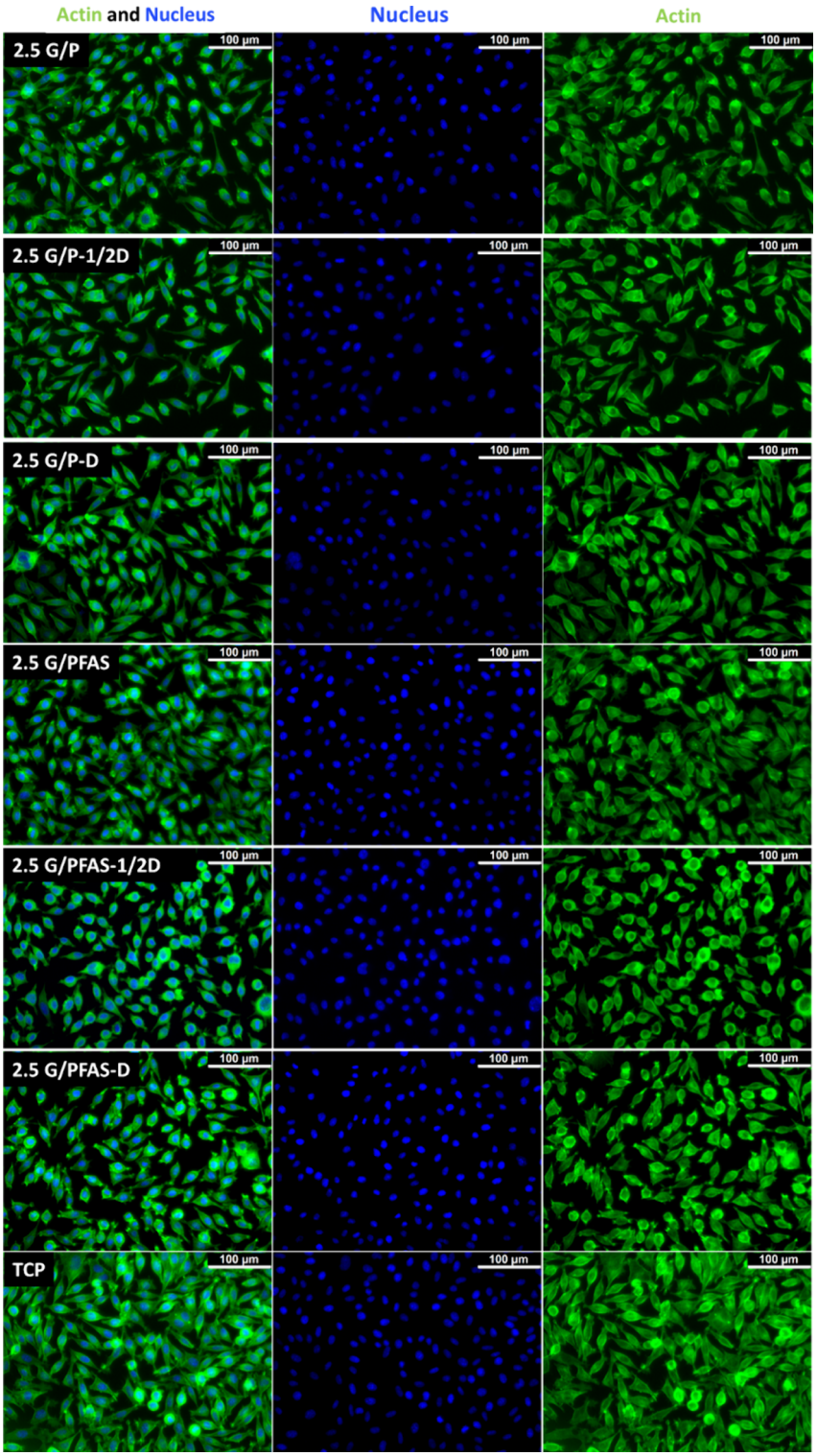

Figure 5. L929 cells cultured for 24 h in contact with sample extracts in comparison with TCP as a control: cellular nucleus in blue (middle column), actin skeleton in green (left column), merged nucleus and actin images (right column), magnification 200×.

temperature 41 °C under actual AMF exposure (Figure 3D–F). To ensure reproducibility, stability, and compatibility with *in vitro* setups, the same temperature profile was subsequently replicated using a controlled oven. This approach allowed us to isolate the thermomagnetic responsive behavior of the system from AMF-equipment variability while maintaining direct consistency with the experimentally validated AMF-induced temperature range. Accordingly, both the thermo-assisted cytotoxicity evaluation (Figure 6) and the ON–OFF release assessment (Figure 7) were conducted under this AMF-equivalent thermal stimulation to provide a reliable, mechanistically grounded *in-vitro* proof-of-concept.

https://doi.org/10.1021/acsami.6c10083
ACS Appl. Mater. Interfaces XXXX, XXX, XXX–XXX

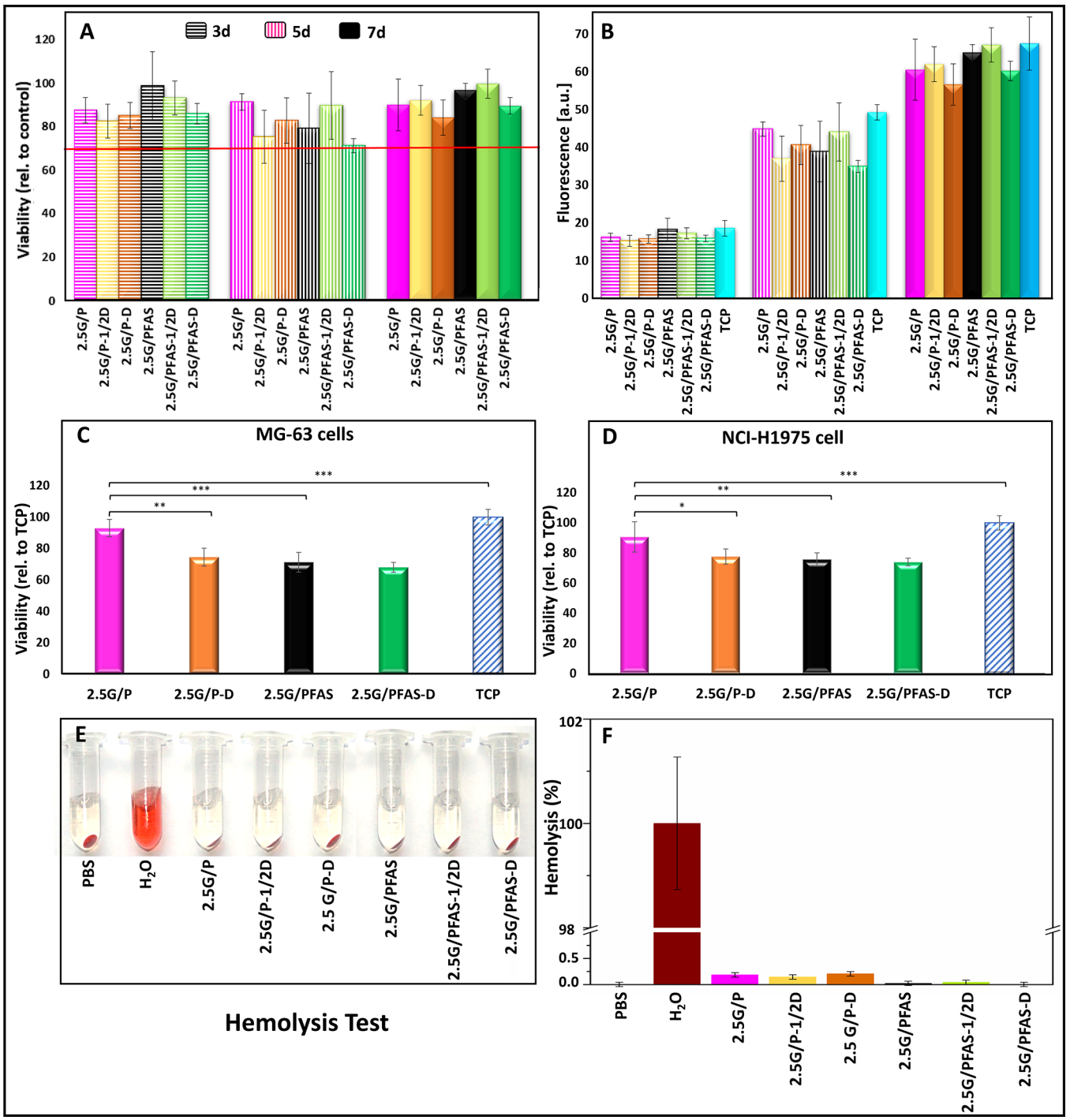

Figure 6. (A) Cell viability in the presence of hydrogels at different time points and (B) corresponding cell absorbance values. (C,D) Viability of human lung adenocarcinoma (NCI-H1975) and fibroblast-like human osteosarcoma (MG-63) cells cultured with the investigated hydrogels. (E,F) Hemolysis ratios and photographs of human RBCs treated with different hydrogel extracts. Statistical significance is indicated as $*p < 0.05$, $**p < 0.01$, and $***p < 0.001$.

The cytotoxicity of the hydrogels was investigated using L929 fibroblasts in a Presto Blue assay. As shown in Figure 6, the addition of different test hydrogel samples did not significantly change cellular viability after 3, 5, and 7 days of incubation in direct contact with the hydrogel samples, with the cell viability exceeding 70% relative to TCP (Figure 6A), and the two-way ANOVA analysis revealed no statistically significant differences (ns). Similarly, an increase in the absorbance of the cells on the 5th and 7th days was observed compared to the 3rd day, suggesting appropriate cell proliferation in contact with the hydrogel and TCP (Figure 6B). This result confirmed the biocompatible potential of the hydrogel and the precursors, hence could act as a drug delivery system for bio-applications.

https://doi.org/10.1021/acsami.6c10083
ACS Appl. Mater. Interfaces XXXX, XXX, XXX–XXX

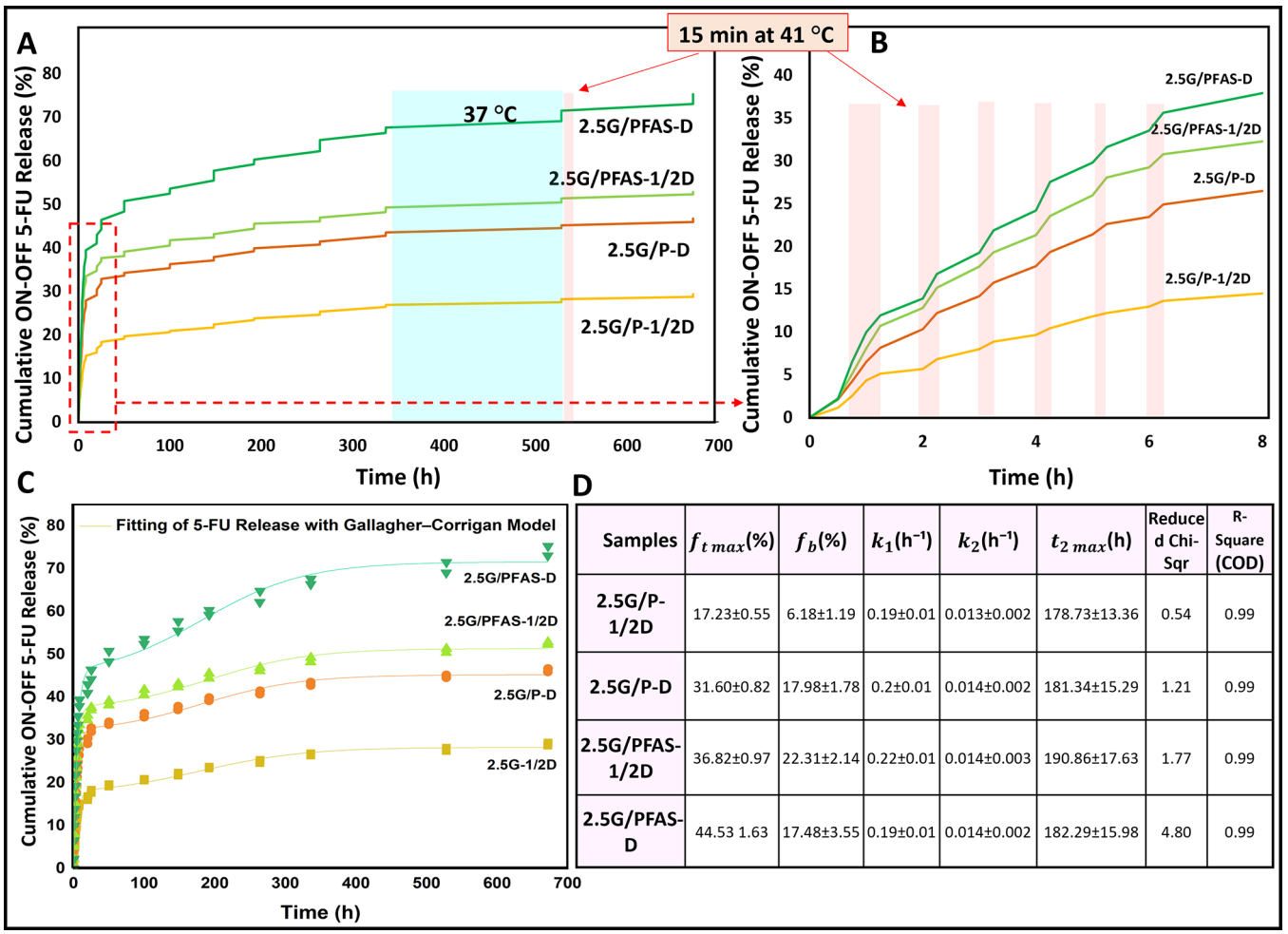

Samples	$f_{t\,max}$(%)	f_b(%)	k_1(h^{-1})	k_2(h^{-1})	$t_{2\,max}$(h)	Reduced Chi-Sqr	R-Square (COD)
2.5G/P-1/2D	17.23±0.55	6.18±1.19	0.19±0.01	0.013±0.002	178.73±13.36	0.54	0.99
2.5G/P-D	31.60±0.82	17.98±1.78	0.2±0.01	0.014±0.002	181.34±15.29	1.21	0.99
2.5G/PFAS-1/2D	36.82±0.97	22.31±2.14	0.22±0.01	0.014±0.003	190.86±17.63	1.77	0.99
2.5G/PFAS-D	44.53 1.63	17.48±3.55	0.19±0.01	0.014±0.002	182.29±15.98	4.80	0.99

Figure 7. (A,B) Drug release profile of the hybrid hydrogels at 37.5 and 41 °C. (C,D) *In vitro* release profiles fitted with the Gallagher–Corrigan model and the corresponding kinetic parameters.

An important criterion for scaffolding in the manufacture of tissue constructs is the maintenance of normal cellular behavior in a 3D microenvironment.[60,61]

In both cell lines-human lung adenocarcinoma (NCI-H1975) and fibroblast-like human osteosarcoma (MG-63)-a reduction in cell viability was observed in the presence of the combined drug and FAS treatment, compared to either the drug or FAS alone, as well as the tissue culture plastic (TCP) control (Figures 6C,D and S3). Before the cell viability analysis, the cells with samples were exposed to heat treatment to simulate the effects of an alternating magnetic field. These results confirm the enhanced anticancer properties of FAS when combined with thermal stimulation.

Blood compatibility and non-cytotoxic properties are critical for hydrogels used in medical applications. The hemolysis ratio test was used to evaluate the blood compatibility of the hydrogels. The positive control, consisting of red blood cells (RBC) dispersed in water, showed bright red after centrifugation, indicating RBC breakage. In contrast, the hydrogel solutions showed a transparent color, which is comparable to the negative control of PBS (Figure 6E,F). All hydrogels exhibited a hemolytic percentage below 2%, which meets ISO 10993-4 requirements, suggesting high blood compatibility. Moreover, scaffolds incorporating FAS did not show any hemolytic influence on human RBCs compared to hydrogels without nanoparticles. Hence, this blood compatibility makes it a suitable candidate for medical applications.

At temperatures above the LCST of PNIPAM (≈32 °C), such as 41 °C used in this study, the swelling ratio decreases, indicating thermally induced shrinkage of the PNIPAM-containing hydrogel. This behavior is consistent with the well-known thermoresponsive mechanism of PNIPAM, where hydrogen bonding between amide groups and water molecules weakens, and hydrophobic interactions between isopropyl groups become dominant, leading to polymer chain collapse.[30]

The switchable release behavior in response to an "ON-OFF" temperature cycle [at (OFF 37.5 °C) and (ON 41 °C)] was further evaluated, with performance correlated to the swelling behavior of the UV-crosslinkable and thermoresponsive hybrid hydrogel (Figure 7). The 5-FU, which is currently the third most used anticancer drug for the treatment of solid cancers, including colorectal and breast, was used as a model drug. The hybrid hydrogel and the FAS-incorporated hybrid hydrogel exhibit an initial burst release within the first 8 h, followed by a slower release phase at 37 °C (Figure 7A,B). When the temperature is increased to 41 °C, the drug release rate increases significantly, indicating temperature-triggered release behavior.

https://doi.org/10.1021/acsami.6c10083
ACS Appl. Mater. Interfaces XXXX, XXX, XXX–XXX

The cumulative release of 5-FU from the hybrid hydrogels at 37.5 °C (control group) and 41.5 °C (test group) gradually increased over time. Hydrogels loaded with 1.0 mg mL^{-1} of 5-FU showed a total cumulative release of 36.5%, compared to 25.8% for 0.5 mg mL^{-1}. The FAS-incorporated hydrogel achieved 72.6% release over 28 days, exhibiting a biphasic pattern with an initial burst followed by sustained release. The release behavior strongly correlated with the temperature-dependent swelling and shrinking of the hydrogels, indicating that 5-FU release was modulated by hydrogel volume changes. Total drug release from 2.5G/PFAS samples is similar to that of other proposed drug carriers analyzed by other researchers. For example, Wu et al. analyzed three sizes of Ag-Au nanoparticle-based carriers loaded with trimetazidine (TMZ drug). The drug loading capacity was a maximum of 46.5 wt % for the biggest nanocarriers. The authors proved that the thicker the gel shell of Ag-Au nanoparticles was, the slower the drug release rate due to the longer restricted diffusion path in the thick gel shell. Additionally, the temperature-dependent drug release profile was presented, also using NIR light as a trigger for on-demand drug release. The experiment was conducted over 48 h, and for the highest analyzed temperature (41 °C), total drug release for all nanocarrier types was 70–80%.[34] Similar drug release kinetics for SPION nanocomposite were presented by Jalili et al.[42]

The release profiles were fitted with the Gallagher–Corrigan model, a biphasic kinetic model commonly applied to complex polymer-based matrices.[62] The model is expressed as:

$$f_t = f_{t\,\max}\left(1 - e^{-k_1 t}\right) + \left(f_{t\,\max} - f_b\right)\cdot\left(\frac{e^{k_2 t - k_2 t_{2\,\max}}}{1 + e^{k_2 t - k_2 t_{2\,\max}}}\right)$$

where f_b is the burst fraction, k_1 and k_2 are the release constants for the initial and sustained phases, respectively, $f_{t\ \max}$ is the maximum fraction released, and $t_{2\ \max}$ is the time at which the transition to the second phase occurs.

The resulting parameters are summarized in Figure 7C,D. The high coefficients of determination ($R^2 = 0.991$–0.994) confirmed the excellent fit of the data. Distinct differences among samples were observed in both the burst fraction (f_b) and the release constants. 2.5G/PFAS-1/2D showed the highest burst release ($f_b = 22.3\%$) and the fastest initial rate ($k_1 = 0.224\ h^{-1}$), indicating a pronounced early release phase, whereas 2.5G/P-1/2D exhibited the lowest burst ($f_b = 6.2\%$) and the most controlled profile. All samples displayed comparable sustained release rates ($k_2 \approx 0.013$–$0.014\ h^{-1}$), suggesting similar long-term release kinetics. Notably, 2.5G/PFAS-D achieved the greatest overall release ($f_{t\ \max} = 44.5\%$), although with a less accurate model fit (Reduced Chi-Sqr = 4.80). These results demonstrate the ability of the Gallagher–Corrigan model to mechanistically distinguish between burst and sustained release phases, providing deeper insight into the release behavior of the formulations.

Although the present study demonstrates promising *in vitro* performance, the absence of in vivo evaluation remains a limitation. Future studies will focus on assessing the biocompatibility, therapeutic efficacy, and long-term stability of the proposed system in relevant animal models to further validate its translational potential.

3. CONCLUSION

A novel, dual-stimuli responsive hybrid hydrogel drug carrier was developed using 2.5% (w/w) gelatin methacryloyl (GelMa) and 5% (w/w) poly(N-isopropylacrylamide) (PNIPAM), integrated with 2% (w/w) folic acid-coated superparamagnetic iron oxide nanoparticles (FAS). The optimized 2.5G/P matrix exhibits exceptional mechanical resilience, achieving a superior compressive strength of 0.06 MPa at 78% strain with excellent shape-memory, ensuring durability under repetitive physiological stress. Furthermore, *in vitro* assays confirmed outstanding cytocompatibility (>70% viability against L929 fibroblasts) and hemocompatibility (hemolysis ratio < 2%, complying with ISO 10993-4 standards), ensuring its safety for contact with blood and physiological fluids. Magnetothermal activation at a hyperthermic temperature of 41 °C induced network shrinkage, triggering a controlled, pulsatile "ON/OFF" release of 5-fluorouracil (5-FU). This release profile, which follows the Gallagher–Corrigan model, reached a maximum cumulative release of 72.6% over 28 days, and yielding a profound synergistic reduction in NCI-H1975 and MG-63 cancer cell viability.

These structural and functional attributes endow the developed 2.5G/P-FAS hydrogel with significant potential for targeted oncological applications. Its injectability and rapid UV-photocrosslinkability make it an ideal candidate for in situ forming, localized drug-delivery implants directly inside post-surgical tumor resections to eradicate residual cancer cells and prevent recurrence. Moreover, its robust compressive stability and blood compatibility allow this thermo-magnetic platform to be engineered as implantable patches for the localized chemo-hyperthermia treatment of solid tumors, such as osteosarcoma and lung malignancies. This work establishes a versatile material platform that paves the way for more precise, patient-tailored, and spatiotemporally controlled cancer therapies.

4. EXPERIMENTAL SECTION

4.1. Materials and Sample Preparation

4.1.1. Raw Materials. Type A gelatin, methacrylic anhydride (MA), *N*-isopropylacrylamide (NIPAM), ethanol (98%), PBS, 2-hydroxy-1-(4-(hydroxyethoxy) phenyl)–2-methyl-1-propanone (Irgacure 2959, IR), *N,N′*-methylenebisacrylamide (BIS), and folic acid were purchased from Sigma-Aldrich. Cut-off dialysis tubing (MWCO: 12–14 kDa) was sourced from Acros Organics and Spectrum Labs. Iron (III) chloride hexahydrate ($FeCl_3{\cdot}6H_2O$), iron (II) chloride tetrahydrate ($FeCl_2{\cdot}4H_2O$), sodium hydroxide (NaOH), acetone, and 25% aqueous ammonia solution (all analytical grade) were supplied by Warchem Sp. z o.o., Warsaw, Poland.

4.1.2. Synthesis of SPIONs and FAS. SPIONs were synthesized via a co-precipitation method. Iron salts, $FeCl_3{\cdot}6H_2O$ (1.08 g, 4.0 mmol) and $FeCl_2{\cdot}4H_2O$ (0.4 g, 2.0 mmol), were dissolved in 50 mL of distilled water [establishing a strict 2:1 stoichiometric molar ratio of Fe^{3+} : Fe^{2+}]. To this, 0.5 mL of 0.1 M HCl was added. The solution was stirred magnetically, and the pH was initially adjusted to 10.5 using an aqueous ammonia solution, then further increased to 11.5. The solution was stirred for an additional 5 min at 80 °C. Afterward, the resulting SPIONs were magnetically separated from the solution, washed thoroughly with distilled water to remove any residual chemicals, and then dried at 60 °C to yield approximately 440 mg of dry nanoparticles.

https://doi.org/10.1021/acsami.6c10083
ACS Appl. Mater. Interfaces XXXX, XXX, XXX–XXX

For FAS, 500 mg of folic acid was dissolved in 40 mL of ethanol/water (4:1) mixture, and the SPION suspension was added to this solution. The pH was again adjusted to 11, and the mixture was stirred at 60 °C for 24 h to facilitate the coating of SPIONs with folic acid. The FAS was purified by centrifugation and then resuspended in distilled water.[50]

4.1.3. Synthesis of GelMa and Thermo-Magnetic Cancer-Treatment Hydrogel Fabrication. GelMa was synthesized by reacting 10 g of Type A gelatin with methacrylic anhydride (MA; 0.8 mL g^{-1} gelatin) in PBS at 60 °C. After the reaction, the mixture was dialyzed against distilled water for 7 days using cut-off dialysis tubing (MWCO: 12–14 kDa) to ensure the complete removal of unreacted methacrylic anhydride. The dialyzed GelMa was subsequently lyophilized to obtain a porous foam.

For the fabrication of hydrogels, GelMa (10% w/w) was dissolved in PBS, and the solution was mixed with (0.5% w/w relative to GelMa) of the photoinitiator Irgacure 2959 (IR). The resulting solution was exposed to UV radiation (365 nm, 12.5 mW cm^{-2}) for 120 s to induce crosslinking and form a hydrogel. For thermoresponsive hydrogels, NIPAM (5% w/w) was added, and BIS (0.2% w/w), FAS (2% w/w), and 5-FU (0.5 and 1% w/w) are accurately described using weight-to-weight percentages (w/w)% based on total polymer mass to ensure clear and replicable formulation protocols,[46] where all monomers and crosslinkers were used as received without further purification.

4.2. Characterization

4.2.1. Morphology. The morphological characteristics of SPIONs, FAS, and hydrogels were analyzed using scanning electron microscopy (SEM; Jeol JSM-6010PLUS/LV InTouchScope) and transmission electron microscopy (TEM; EF-TEM, Zeiss Libra 120 Plus). For SEM imaging, samples were sputter-coated with gold to enhance conductivity.

4.2.2. Chemical Structure. Fourier-transform infrared spectroscopy (FTIR; Bruker Vertex 70 FT-IR Spectroscopy).

4.2.3. Thermal Properties. The thermal characterization and stability of the hydrogels were assessed using differential scanning calorimetry (DSC; Perkin Elmer PYRIS-1) and thermogravimetric analysis (TGA; TGA 8000, Perkin Elmer).

4.2.4. Magnetic Properties. The magnetic response of both SPIONs and FAS hydrogels was evaluated using vibrating sample magnetometry (VSM; QD vibrating sample magnetometer VSM) to assess their superparamagnetic behavior.

4.2.5. Mechanical Properties. Compression Testing: The mechanical properties of the hydrogels were evaluated through compression tests conducted using a texture analyzer (Brookfield Ametek CTX TA) at a compression rate of 1 mm/min.

4.2.6. Swelling Ratio. The swelling behavior of the hydrogels was studied by immersing dried hydrogel samples in distilled water at room temperature (25 °C). The weight of the samples was measured at several time points (0.25, 0.5, 1, 2, 3, 6, and 24 h) to evaluate the swelling kinetics.

4.2.7. Magnetic Hyperthermia Studies. The heat was induced using 10KWHF equipment supplied from the Superior Induction Company (Pasadena, CA, USA) using amplitude in the range 27–35 Gauss (G) and frequency about 294 kHz (using copper solenoid type with coils number: 7, height: 5 cm, diameter: 7 cm). The heating effectiveness of the hydrogel was recorded using a FLIR A300 thermovision camera.

4.3. Biological Evaluations

4.3.1. Cytotoxicity. Cellular viability was assessed using the PrestoBlue assay on L929 fibroblasts (Sigma-Aldrich). Cells were seeded in 96-well plates and incubated with the hydrogel extracts for 2, 5, and 7 days to evaluate any cytotoxic effects.

4.3.2. Sterilization Process. Prior to conducting the subsequent four analyses, the prepared hydrogels were washed for a duration of 10 days. This extended washing period was implemented to ensure the complete removal of any unreacted monomers, cross-linking agents, solvents, or other potentially toxic residues from the synthesis process. Following this, the material samples were sterilized under UV radiation for 30 min before proceeding with the cell loading and hemolysis assays.

4.3.3. Cell Morphology. Fibroblast morphology following exposure to extracts was analyzed via fluorescence microscopy. The cytoskeleton and nuclei were stained using ActinGreen and NucBlue, respectively. Microscopic images were acquired at 200× magnification using a Leica AM TIRF MC microscope.

4.3.4. Anticancer Tests. On the starting day of the experiment, the human lung adenocarcinoma cell line NCI-H1975 (ATCC) and fibroblast-like human osteosarcoma cell line MG-63 (Sigma-Aldrich) cells were detached using trypsin and seeded at a density of 10,000 cells per well into 48-well plates, separately for each cell type. The following day, samples were added: 2.5G/P, 2.5G/P-D, 2.5G/PFAS, and 2.5G/PFAS-D. The next day, 48-well plates containing the cells and samples were exposed to thermal treatment: 5 cycles of 15 min at 41 °C, with 5-min breaks at 37 °C between each cycle. After 2 days, a PrestoBlue assay was performed to assess cell viability.

4.3.5. Hemolysis Assay. Extracts were prepared from 8 mg of each sample type. The samples were immersed in 2 mL of PBS, kept at 37 °C, and gently stirred for 24 h.[4] Fresh, healthy human blood was collected using Vacuette tubes containing sodium citrate as an anticoagulant (9 mL; Greiner Bio-One, Frickenhausen, Germany). Whole blood was diluted with PBS at a 1:2 volume ratio. The RBCs were then separated from the plasma by centrifuging at 500 g for 10 min and washed five times with 10 mL of PBS. For the hemolysis test, 0.2 mL of the diluted RBC suspension (around 5×10^8 cells per mL) was added to 0.8 mL of non-diluted extracts. The RBC suspension dispersed in PBS was selected as a negative control and the RBCs suspension dispersed in distilled water was used as a positive control. All the suspensions were centrifuged at 10,000 g for 3 min after incubation at 37 °C for 3 h. The absorbance of the resulting supernatant was measured at 540 nm using a microplate reader (Synergy HTX, BioTek, Winooski, VT, USA). The hemolysis rate was calculated according to the following equation:

$$\text{Percentage of hemolysis} = \frac{\text{sample absorbance} - \text{negative control absorbance}}{\text{positive control absorbance} - \text{negative control absorbance}} \times 100\%$$

4.3.6. Drug Release. The release of the chemotherapy drug 5-FU from the thermoresponsive hydrogels was investigated under an ON-OFF temperature-controlled system using ovens, which was employed to simulate the thermal effects of an AMF. The temperature was alternated between 37.5 °C (OFF), representing the normal drug release condition, with sampling at multiple time points (0.5, 1, 2, 3, 4, 5, 6, 8, 20, 25, 50, 100, 148, 192, 264, 336, 528, and 672 h) and 41.5 °C as simulated hyperthermia point (ON for 15 min), which was applied between each interval at 37.5 °C as part of a thermal switching protocol. The amount of released 5-FU was quantified using a UV absorption spectrophotometer (Multiscan GO, Thermo Scientific) at 285 nm.

4.3.7. Statistical Analysis. All experimental data were expressed as the mean ± standard deviation (SD). Statistical significance was evaluated using GraphPad Prism 8.0.1 software. A p-value of less than 0.05 was considered statistically significant. Two-way ANOVA with Tukey's multiple comparison test was used, where applicable, to compare groups.

■ ASSOCIATED CONTENT

Supporting Information

The supporting information is available free of charge at https://pubs.acs.org/doi/10.1021/acsami.6c10083.

https://doi.org/10.1021/acsami.6c10083
ACS Appl. Mater. Interfaces XXXX, XXX, XXX–XXX

Additional experimental details, H-NMR spectral signals of GelMa and gelatin (Figure S1), SEM images of SPIONs and FAS (Figure S2), and preliminary analysis of multicomponent hydrogels and evaluation of cellular activity (Figure S3) (DOCX)

AUTHOR INFORMATION

Corresponding Author

Paweł Sajkiewicz – *Laboratory of Polymers and Biomaterials, Institute of Fundamental Technological Research, Polish Academy of Sciences, Pawińskiego 5b, Warsaw 02-106, Poland*; orcid.org/0000-0003-4092-9853; Email: psajk@ippt.pan.pl

Authors

Zahra Moazzami Goudarzi – *Laboratory of Polymers and Biomaterials, Institute of Fundamental Technological Research, Polish Academy of Sciences, Pawińskiego 5b, Warsaw 02-106, Poland*; orcid.org/0000-0001-9168-3932

Sohrab Asgaran – *Helmaco Sp. Z o.o. Company, Ostrobramska 101/335K, Warszawa 04-041, Poland*; orcid.org/0009-0004-0528-6260

Magdalena Osial – *Department of Theory of Continuous Media and Nanostructures, Institute of Fundamental Technological Research, Polish Academy of Sciences, Pawińskiego 5b, Warsaw 02-106, Poland*

Njemuwa Nwaji – *Department of Theory of Continuous Media and Nanostructures, Institute of Fundamental Technological Research, Polish Academy of Sciences, Pawińskiego 5b, Warsaw 02-106, Poland*; orcid.org/0000-0003-2350-1396

Dorota Kołbuk – *Laboratory of Polymers and Biomaterials, Institute of Fundamental Technological Research, Polish Academy of Sciences, Pawińskiego 5b, Warsaw 02-106, Poland*

Arkadiusz Gradys – *Laboratory of Polymers and Biomaterials, Institute of Fundamental Technological Research, Polish Academy of Sciences, Pawińskiego 5b, Warsaw 02-106, Poland*

Bartlomiej Kalaska – *Department of Pharmacodynamics, Medical University of Bialystok, Mickiewicza 2c, Bialystok 15-089, Poland*; orcid.org/0000-0002-4968-4429

Olga Urbanek – *Laboratory of Polymers and Biomaterials, Institute of Fundamental Technological Research, Polish Academy of Sciences, Pawińskiego 5b, Warsaw 02-106, Poland*; orcid.org/0000-0002-1920-9715

Complete contact information is available at: https://pubs.acs.org/doi/10.1021/acsami.6c10083

Author Contributions

Z.M.G.: Conceptualization, methodology, analysis, investigation, writing—original draft, writing—review & editing. S.A.: Analysis, investigation, writing—review & editing. M.O.: Analysis, investigation, writing—review & editing. N.N.: Analysis, investigation, writing—review & editing. D.K.: Analysis, investigation, writing—review & editing. A.G.: Analysis, investigation, writing—review & editing. B.K.: Analysis, investigation, writing—review & editing. O.U.: Review, editing & funding acquisition. P.S.: Review, editing & funding acquisition.

Notes

The human blood collection procedure was approved by the Bioethics Committee of the Medical University of Bialystok, Poland (Permit Number APK.002.530.2023).
The authors declare no competing financial interest.

ACKNOWLEDGMENTS

This work received financial support from the National Science Centre, Poland, under the SONATA program (Grant No. 2022/47/D/ST5/01395) awarded to Z.MG. and O.U. Additionally, O.U. gratefully acknowledges the financial support from the Polish Ministry of Science and Higher Education through scholarships for outstanding young scientists (Decision No. SMN/18/1755/2022). M.O. would like to acknowledge the additional support from the National Science Centre of Poland (grant 2023/51/D/NZ7/01557).

REFERENCES

(1) National Cancer Institute. *SEER Cancer Statistics AC:FSEER Cancer Statistics Factsheets: Common Cancer Sitesactsheets: Common Cancer Sites*; National Institutes of Health: Bethesda, MD, **2024**. https://seer.cancer.gov/statfacts/html/common.html (accessed July 2026).

(2) Gong, Z.; Zhou, D.; Wu, D.; Han, Y.; Yu, H.; Shen, H.; Feng, W.; Hou, L.; Chen, Y.; Xu, T. Challenges and Material Innovations in Drug Delivery to Central Nervous System Tumors. *Biomaterials* **2025**, *319*, 123180.

(3) Goudarzi, Z. M.; Soleimani, M.; Ghasemi-Mobarakeh, L.; Sajkiewicz, P.; Sharifianjazi, F.; Esmaeilkhanian, A.; Khaksar, S. Control of Drug Release from Cotton Fabric by Nanofibrous Mat. *Int. J. Biol. Macromol.* **2022**, *217*, 270–281.

(4) Amarjargal, A.; Moazzami Goudarzi, Z.; Cegielska, O.; Gradys, A.; Kolbuk, D.; Kalaska, B.; Ruszczyńska, A.; Sajkiewicz, P. A Facile One-Stone-Two-Birds Strategy for Fabricating Multifunctional 3D Nanofibrous Scaffolds. *Biomater. Sci.* **2023**, 5502–5516.

(5) Fenton, O. S.; Olafson, K. N.; Pillai, P. S.; Mitchell, M. J.; Langer, R. Advances in Biomaterials for Drug Delivery. *Adv. Mater.* **2018**, *30* (29).

(6) Fariborz Sharifianjazi, Amirhossein Esmaeilkhanian, Mehdi Reisi Nafchi, Leila Bazli, Pouran Pourhakkak, Hosein Rostamani, Mohammad Yusuf, Zahra Moazzami Goudarzi, Samad Khaksar, A. F. Manufacturing of Nanocomposites by Electrospinning. In *Chemical Physics of Polymer Nanocomposites: Processing, Morphology, Structure, Thermodynamics, Rheology*; Vera V. Myasoedova, Sabu Thomas, H. J. M., Ed.; WILEY-VCH GmbH; pp 67–94.

(7) Moazzami Goudarzi, Z.; Behzad, T.; Ghasemi-Mobarakeh, L.; Kharaziha, M.; Enayati, M. S. Structural and Mechanical Properties of Fibrous Poly (Caprolactone)/Gelatin Nanocomposite Incorporated with Cellulose Nanofibers. *Polym. Bull.* **2020**, *77* (2), 717–740.

(8) Moazzami Goudarzi, Z.; Behzad, T.; Ghasemi-Mobarakeh, L.; Kharaziha, M. An Investigation into Influence of Acetylated Cellulose Nanofibers on Properties of PCL/Gelatin Electrospun Nanofibrous Scaffold for Soft Tissue Engineering *Polymer (Guildf)*. **2021**, *213*, 123313

(9) Zolfagharlou Kouhi, M.; Behzad, T.; Ghasemi-Mobarakeh, L.; Allafchian, A.; Moazzami Goudarzi, Z.; Enayati, M. S. Proceeding toward the Development of Poly(ε-Caprolactone)/Cellulose Microfibrils Electrospun Biocomposites Using a Novel Ternary Solvent System. *J. Text. Inst.* **2020**, *111* (2), 249–259.

(10) Dong, S.; An, S.; Saiding, Q.; Chen, Q.; Liu, B.; Kong, N.; Chen, W.; Tao, W. Therapeutic Hydrogels: Properties and Biomedical Applications. *Chem. Rev.* **2025**, 8835–8920.

(11) Maity, S.; Mahata, K.; Meshram, B.; Banerjee, S. Smart Polymer-Derived Injectable Hydrogels: Current Status and Future Perspectives. *ACS Polym. Au* **2025**, 680–711.

(12) Śliwa, T.; Jarzębski, M.; Gapiński, J.; Grzeszkowiak, M.; Kleshchanok, D. Stimuli-Responsive PNIPAM Based Copolymers: Modeling and Light Scattering Investigations. *Acta Phys. Pol., A* **2014**, *125* (5), 1236–1239.
(13) Dutta, S.; Samanta, P.; Dhara, D. Temperature, PH and Redox Responsive Cellulose Based Hydrogels for Protein Delivery. *Int. J. Biol. Macromol.* **2016**, *87*, 92–100.
(14) Riedinger, A.; Pernia Leal, M.; Deka, S. R.; George, C.; Franchini, I. R.; Falqui, A.; Cingolani, R.; Pellegrino, T. nanohybrids" Based on PH-Responsive Hydrogels and Inorganic Nanoparticles for Drug Delivery and Sensor Applications. *Nano Lett.* **2011**, *11* (8), 3136–3141.
(15) Moazzami Goudarzi, Z.; Zaszczyńska, A.; Kowalczyk, T.; Sajkiewicz, P. Electrospun Antimicrobial Drug Delivery Systems and Hydrogels Used for Wound Dressings. *Pharmaceutics* **2024**, *16* (1).
(16) Badeau, B. A.; Deforest, C. A. Programming Stimuli-Responsive Behavior into Biomaterials. *Annu. Rev. Biomed. Eng.* **2019**, *21*, 241–265.
(17) Hou, L.; Wu, P. Comparison of LCST-Transitions of Homopolymer Mixture, Diblock and Statistical Copolymers of NIPAM and VCL in Water. *Soft Matter* **2015**, *11* (14), 2771–2781.
(18) Heyda, J.; Muzdalo, A.; Dzubiella, J. Rationalizing Polymer Swelling and Collapse under Attractive Cosolvent Conditions. *Macromolecules* **2013**, *46* (3), 1231–1238.
(19) Zhang, Y.; Wang, P.; Chen, R. Effect of the Macromolecular Architecture on the Thermoresponsive Behavior of Poly(N-Isopropylacrylamide) in Copolymers with Poly(N,N-Dimethylacrylamide) in Aqueous Solutions: Block vs Random Copolymers. *React. Funct. Polym.* **2022**, *171*, 105150.
(20) Santhamoorthy, M.; Vy Phan, T. T.; Ramkumar, V.; Raorane, C. J.; Thirupathi, K.; Kim, S. C. Thermo-Sensitive Poly (N-Isopropylacrylamide-Co-Polyacrylamide) Hydrogel for PH-Responsive Therapeutic Delivery. *Polymers (Basel)*. **2022**, *14* (19).
(21) Mohammed, A. M.; Osman, S. K.; Saleh, K. I.; Samy, A. M. In Vitro Release of 5-Fluorouracil and Methotrexate from Different Thermosensitive Chitosan Hydrogel Systems. *AAPS PharmSciTech* **2020**, *21* (4), 1–11.
(22) Zakerikhoob, M.; Abbasi, S.; Yousefi, G.; Mokhtari, M.; Noorbakhsh, M. S. Curcumin-Incorporated Crosslinked Sodium Alginate-g-Poly (N-Isopropyl Acrylamide) Thermo-Responsive Hydrogel as an in-Situ Forming Injectable Dressing for Wound Healing: In Vitro Characterization and in Vivo Evaluation. *Carbohydr. Polym.* **2021**, *271*, 118434.
(23) Wong, J. E.; Krishnakumar Gaharwar, A.; Müller-Schulte, D.; Bahadur, D.; Richtering, W. Layer-by-Layer Assembly of a Magnetic Nanoparticle Shell on a Thermoresponsive Microgel Core. *J. Magn. Magn. Mater.* **2007**, *311* (1 SPEC. ISS.), 219–223.
(24) Li, S.; Wang, W.; Li, W.; Xie, M.; Deng, C.; Sun, X.; Wang, C.; Liu, Y.; Shi, G.; Xu, Y.; Ma, X.; Wang, J. Fabrication of Thermoresponsive Hydrogel Scaffolds with Engineered Microscale Vasculatures. *Adv. Funct. Mater.* **2021**, *31* (27).
(25) Zhu, Y.; Yu, X.; Liu, H.; Li, J.; Gholipourmalekabadi, M.; Lin, K.; Yuan, C.; Wang, P. Strategies of Functionalized GelMA-Based Bioinks for Bone Regeneration: Recent Advances and Future Perspectives. *Bioact. Mater.* **2024**, *38*, 346–373.
(26) Dong, Z.; Yuan, Q.; Huang, K.; Xu, W.; Liu, G.; Gu, Z. Gelatin Methacryloyl (GelMA)-Based Biomaterials for Bone Regeneration. *RSC Adv.* **2019**, *9* (31), 17737–17744.
(27) Samimi Gharaie, S.; Dabiri, S. M. H.; Akbari, M. Smart Shear-Thinning Hydrogels as Injectable Drug Delivery Systems. *Polymers (Basel)* **2018**, *10* (12), 1317.
(28) Mamidi, N.; Ijadi, F.; Norahan, M. H. Leveraging the Recent Advancements in GelMA Scaffolds for Bone Tissue Engineering: An Assessment of Challenges and Opportunities. *Biomacromolecules* **2024**, *25* (4), 2075–2113.
(29) Huang, Y. C.; Cheng, Q. P.; Jeng, U. S.; Hsu, S. H. A Biomimetic Bilayer Hydrogel Actuator Based on Thermoresponsive Gelatin Methacryloyl-Poly(N-Isopropylacrylamide) Hydrogel with Three-Dimensional Printability. *ACS Appl. Mater. Interfaces* **2023**, *15* (4), 5798–5810.
(30) Daaboul, M.; Akkaya, A.; Kanli, Z.; Gunduz, O.; Aydın, B.; Alarcin, E.; Ozmen, M. M.; Topuzogullari, M. Nanoparticle-Embedded GelMA/NIPAm Hydrogels: A Temperature-Responsive Hybrid System for Controlled Drug Release. *Macromol. Biosci.* **2025**, *26*, e00635.
(31) Liu, C.; Meng, M.; Yang, Z.; Wu, S.; Shang, L.; Feng, Y.; Wu, J.; Hao, K.; Wang, R.; Zhou, D.; He, S.; Li, Y.; Tian, H. Magnetic Polymer Microcarriers for Cell Engineering Applications with Enzyme-Free Cell Harvesting and Rapid Recovery in Large-Scale Cell Culture. *Adv. Funct. Mater.* **2024**, *34* (11).
(32) Zhao, X.; Liu, Y.; Shao, C.; Nie, M.; Huang, Q.; Li, J.; Sun, L.; Zhao, Y. Photoresponsive Delivery Microcarriers for Tissue Defects Repair. *Adv. Sci.* **2019**, *6* (20).
(33) Wang, J.; Huang, D.; Ren, H.; Shang, L. Biomimic Trained Immunity-MSCs Delivery Microcarriers for Acute Liver Failure Regeneration. *Small* **2022**, *18* (36), e2200858.
(34) Wu, W.; Shen, J.; Banerjee, P.; Zhou, S. Core-Shell Hybrid Nanogels for Integration of Optical Temperature-Sensing, Targeted Tumor Cell Imaging, and Combined Chemo-Photothermal Treatment. *Biomaterials* **2010**, *31* (29), 7555–7566.
(35) Zhao, X. Q.; Wang, T. X.; Liu, W.; Wang, C. D.; Wang, D.; Shang, T.; Shen, L. H.; Ren, L. Multifunctional Au@IPN-PNIPAAm Nanogels for Cancer Cell Imaging and Combined Chemo-Photothermal Treatment. *J. Mater. Chem.* **2011**, *21* (20), 7240–7247.
(36) Chiang, W. H.; Ho, V. T.; Chen, H. H.; Huang, W. C.; Huang, Y. F.; Lin, S. C.; Chern, C. S.; Chiu, H. C. Superparamagnetic Hollow Hybrid Nanogels as a Potential Guidable Vehicle System of Stimuli-Mediated MR Imaging and Multiple Cancer Therapeutics. *Langmuir* **2013**, *29* (21), 6434–6443.
(37) Deka, S. R.; Quarta, A.; Di-Corato, R.; Falqui, A.; Manna, L.; Cingolani, R.; Pellegrino, T. Acidic PH-Responsive Nanogels as Smart Cargo Systems for the Simultaneous Loading and Release of Short Oligonucleotides and Magnetic Nanoparticles. *Langmuir* **2010**, *26* (12), 10315–10324.
(38) Dulińska-Litewka, L.; Łazarczyk, A.; Hałubiec, P.; Szafrański, O.; Karnas, K.; Karewicz, A. Superparamagnetic Iron Oxide Nanoparticles—Current and Prospective Medical Applications, *Materials (Basel)* **2019**, *12*, 617.
(39) Dias, A. M. M.; Courteau, A.; Bellaye, P.-S.; Kohli, E.; Oudot, A.; Doulain, P.-E.; Petitot, C.; Walker, P.-M.; Decréau, R.; Collin, B. Superparamagnetic Iron Oxide Nanoparticles for Immunotherapy of Cancers through Macrophages and Magnetic Hyperthermia. *Pharmaceutics* **2022**, *14* (11).
(40) Dagdelen, S.; Mackiewicz, M.; Osial, M.; Waleka-Bargiel, E.; Romanski, J.; Krysinski, P.; Karbarz, M. Redox-Responsive Degradable Microgel Modified with Superparamagnetic Nanoparticles Exhibiting Controlled, Hyperthermia-Enhanced Drug Release. *J. Mater. Sci.* **2023**, *58* (9), 4094–4114.
(41) Hoare, T.; Santamaria, J.; Goya, G. F.; Irusta, S.; Lin, D.; Lau, S.; Padera, R.; Langer, R.; Kohane, D. S. A Magnetically Triggered Composite Membrane for On-Demand Drug Delivery. *Nano Lett.* **2009**, *9* (10), 3651–3657.
(42) Jalili, N. A.; Jaiswal, M. K.; Peak, C. W.; Cross, L. M.; Gaharwar, A. K. Injectable Nanoengineered Stimuli-Responsive Hydrogels for on-Demand and Localized Therapeutic Delivery. *Nanoscale* **2017**, *9* (40), 15379–15389.
(43) Campbell, S. B.; Patenaude, M.; Hoare, T. Injectable Superparamagnets: Highly Elastic and Degradable Poly(N-Isopropylacrylamide)-Superparamagnetic Iron Oxide Nanoparticle (SPION) Composite Hydrogels. *Biomacromolecules* **2013**, *14* (3), 644–653.
(44) Campbell, S.; Maitland, D.; Hoare, T. Enhanced Pulsatile Drug Release from Injectable Magnetic Hydrogels with Embedded Thermosensitive Microgels. *ACS Macro Lett.* **2015**, *4* (3), 312–316.
(45) Bulcke, A. I., Van Den; Bogdanov, B.; Rooze, N., De; Schacht, E. H.; Cornelissen, M.; Berghmans, H. Structural and Rheological

https://doi.org/10.1021/acsami.6c10083
ACS Appl. Mater. Interfaces XXXX, XXX, XXX–XXX

Properties of Methacrylamide Modified Gelatin Hydrogels. *Biomacromolecules* **2000**, *1* (1), 31–38.
(46) Celikkin, N.; Mastrogiacomo, S.; Jaroszewicz, J.; Walboomers, X. F.; Swieszkowski, W. Gelatin Methacrylate Scaffold for Bone Tissue Engineering: The Influence of Polymer Concentration. *J. Biomed. Mater. Res. A* **2018**, *106* (1), 201–209.
(47) Thakur, T.; Xavier, J. R.; Cross, L.; Jaiswal, M. K.; Mondragon, E.; Kaunas, R.; Gaharwar, A. K. Photocrosslinkable and Elastomeric Hydrogels for Bone Regeneration. *J. Biomed. Mater. Res. A* **2016**, *104* (4), 879–888.
(48) Li, B.; Kennedy, J. F.; Jiang, Q. G.; Xie, B. J. Quick Dissolvable, Edible and Heatsealable Blend Films Based on Konjac Glucomannan - Gelatin. *Food Res. Int.* **2006**, *39* (5), 544–549.
(49) Podewitz, M.; Wang, Y.; Quoika, P. K.; Loeffler, J. R.; Schauperl, M.; Liedl, K. R. Coil-Globule Transition Thermodynamics of Poly(N-Isopropylacrylamide). *J. Phys. Chem. B* **2019**, *123* (41), 8838–8847.
(50) Thanh, D. T. M.; Phuong, N. T.; Hai, D. T.; Giang, H. N.; Thom, N. T.; Nam, P. T.; Dung, N. T.; Giersig, M.; Osial, M. Influence of Experimental Conditions during Synthesis on the Physicochemical Properties of the SPION/Hydroxyapatite Nanocomposite for Magnetic Hyperthermia Application. *Magnetochemistry* **2022**, *8* (8), 90.
(51) Reguieg, F.; Ricci, L.; Bouyacoub, N.; Belbachir, M.; Bertoldo, M. Thermal Characterization by DSC and TGA Analyses of PVA Hydrogels with Organic and Sodium MMT. *Polym. Bull.* **2020**, *77* (2), 929–948.
(52) Gneveckow, U.; Jordan, A.; Scholz, R.; Brüß, V.; Waldöfner, N.; Ricke, J.; Feussner, A.; Hildebrandt, B.; Rau, B.; Wust, P. Description and Characterization of the Novel Hyperthermia- and Thermoablation-System MFH®300F for Clinical Magnetic Fluid Hyperthermia. *Med. Phys.* **2004**, *31* (6), 1444–1451.
(53) Mahmoudi, K.; Bouras, A.; Bozec, D.; Ivkov, R.; Hadjipanayis, C. Magnetic Hyperthermia Therapy for the Treatment of Glioblastoma: A Review of the Therapy's History, Efficacy and Application in Humans. *Int. J. Hyperthermia* **2018**, *34* (8), 1316–1328.
(54) Dhar, D.; Ghosh, S.; Das, S.; Chatterjee, J. A Review of Recent Advances in Magnetic Nanoparticle-Based Theranostics of Glioblastoma. *Nanomedicine* **2022**, 107–132.
(55) Halperin, A.; Kröger, M.; Winnik, F. M. Poly(N-Isopropylacrylamide) Phase Diagrams: Fifty Years of Research. *Angew. Chem., Int. Ed.* **2015**, *54* (51), 15342–15367.
(56) Rabini, A.; Piazzini, D. B.; et al. Deep Heating Therapy via Microwave Diathermy Relieves Pain and Improves Physical Function in Patients with Knee Osteoarthritis: A Double-Blind Randomized Clinical Trial, *Eur. J. Phys. Rehab. Med.* **2012**, *48*, 549.
(57) Frasca, G.; Maggi, L.; Padua, L.; Ferrara, P. E.; Granata, G.; Minciotti, I.; Marzetti, E.; Specchia, A.; Ronconi, G.; Rabini, A.; Bertolini, C.; Piazzini, D. B. Short-Term Effects of Local Microwave Hyperthermia on Pain and Function in Patients with Mild to Moderate Carpal Tunnel Syndrome: A Double Blind Randomized Sham-Controlled Trial. *Clin. Rehabil.* **2011**, *25* (12), 1109–1118.
(58) Cohen, N. Programming the Equilibrium Swelling Response of Heterogeneous Polymeric Gels *Int. J. Solids Struct.* **2019**, *178–179*, 81–90
(59) Yanfeng, C.; Min, Y. Swelling Kinetics and Stimuli-Responsiveness of Poly(DMAEMA) Hydrogels Prepared by UV-Irradiation. *Radiat. Phys. Chem.* **2001**, *61* (1), 65–68.
(60) Lutolf, M. P.; Gilbert, P. M.; Blau, H. M. Designing Materials to Direct Stem-Cell Fate. *Nature* **2009**, *462* (7272), 433–441.
(61) Matshitse, R.; Nwaji, N.; Mananga, M.; Prinsloo, E.; Nyokong, T. Effect of Number of Positive Charges on the Photophysical and Photodynamic Therapy Activities of Quarternary Benzothiazole Substituted Zinc Phthalocyanine. *J. Photochem. Photobiol. A Chem.* **2018**, *367*, 253–260.
(62) Balcerzak, J.; Mucha, M. Analysis of Model Drug Release Kinetics from Complex Matrices of Polylactide-Chitosan. *Prog. Chem. Appl. Chitin Deriv.* **2010**, *XV* (15), 117–126.

https://doi.org/10.1021/acsami.6c10083
ACS Appl. Mater. Interfaces XXXX, XXX, XXX–XXX